First-principles study of iron spin crossover in the new hexagonal aluminous phase

Han Hsu[*]

Department of Physics, National Central University, Taoyuan City 32001, Taiwan
(Received 18 November 2016; published 6 January 2017)

The new hexagonal aluminous (NAL) phase, chemical formula $AB_2C_6O_{12}$ ($A = $ Na$^+$, K$^+$, Ca^{2+}; $B = $ Mg^{2+}, Fe^{2+}, Fe^{3+}; $C = $ Al^{3+}, Si^{4+}, Fe^{3+}), is considered a major component ($\sim$20 vol%) of mid-ocean ridge basalt (MORB) under the lower-mantle condition. As MORB can be transported back into the Earth's lower mantle via subduction, a thorough knowledge of the NAL phase is essential to fully understand the fate of subducted MORB and its role in mantle dynamics and heterogeneity. In this Rapid Communication, the complicated spin crossover of the Fe-bearing NAL phase is revealed by a series of local density approximation + self-consistent Hubbard U (LDA+U_{sc}) calculations. Only the ferric iron (Fe^{3+}) substituting Al/Si in the octahedral (C) site undergoes a crossover from the high-spin (HS) to the low-spin (LS) state at $\sim$40 GPa, while iron substituting Mg in the trigonal-prismatic (B) site remains in the HS state, regardless of its oxidation state (Fe^{2+} or Fe^{3+}). The volume/elastic anomalies and the iron nuclear quadrupole splittings determined by calculations are in great agreement with room-temperature experiments. The calculations further predict that the HS-LS transition pressure of the NAL phase barely increases with temperature due to the three nearly degenerate LS states of Fe^{3+}, suggesting that the elastic anomalies of this mineral can occur at the top lower mantle.

Iron, the most abundant transition metal in the Earth, is incorporated in many minerals. Due to its incomplete 3d shell, iron in many minerals is subject to spin crossover (SCO): The total electron spin S varies with pressure, temperature, strain, and chemical environment. Extensive studies on ferropericlase [(Mg,Fe)O], which constitutes $\sim$20 vol% of the Earth's lower mantle (660–2890 km deep, pressure range 23–135 GPa), have shown that SCO directly affects the structural, electronic, optical, elastic, and thermodynamic properties of the host mineral, iron diffusion, iron partitioning, and thus mantle properties [1–18]. SCO in other lower-mantle minerals has also been reported, including Fe-bearing MgSiO$_3$ perovskite (also known as bridgmanite), which is the most abundant mineral in the Earth [14–25], and (Mg,Fe)CO$_3$ ferromagnesite, which is believed to be the major carbon carrier in the lower mantle [26–35]. Geophysical and geochemical effects of SCO have thus been highly anticipated [13,16,17].

Recently, one more lower-mantle mineral, the new hexagonal aluminous (NAL) phase, is reported to show signatures of SCO under compression [36]. The NAL phase is contained in mid-ocean ridge basalt (MORB), which is formed by partial melting of the upper-mantle peridotite along the mid-ocean ridge. MORB can be transported back into the Earth's lower mantle via subduction, supplying the lower mantle with colder and chemically distinct materials, making this region thermally and chemically heterogeneous. Given its role in mantle dynamics and heterogeneity, the fate of subducted MORB has been a major subject in geoscience [37–41]. In the lower mantle, MORB is believed to contain two aluminum hosts [42–54]: (1) The NAL phase, which is a product of garnet decomposition at $\sim$25 GPa and remains stable up to 50–60 GPa, and (2) the calcium-ferrite-type (CF) phase, which is considered the high-pressure phase of the NAL phase and remains stable up to 85–90 GPa [51–54]. These two aluminous phases, distinct from the major lower-mantle mineral phases

(bridgmanite and ferropericlase), constitute 20–30 vol% of MORB [53,54]. A thorough knowledge of these aluminous phases is thus essential to fully understand the fate of subducted MORB. Most studies, however, are only focused on Fe-free cases [42–52]. Considering the newly discovered SCO in the Fe-bearing NAL phase and the complicated nature of this mineral, comprehensive computational work is necessary.

The NAL phase ($P6_3/m$ symmetry, space group 176) has a chemical formula of $AB_2C_6O_{12}$ (21-atom unit cell), with the nine-coordinated (A) site occupied by large cations (Na$^+$, K$^+$, or Ca^{2+}), the trigonal-prismatic (B) site occupied by Mg^{2+}, and the octahedral (C) site occupied by small cations (Al^{3+}, Si^{4+}). The CO_6 octahedra are arranged in double chains extending along the [001] direction (see Supplemental Material [55] or Fig. 1). In natural MORB, the NAL phase mainly consists of Na, Mg, Al, Si, and O, with a ratio of approximately 1:2:5:1:12, and a small amount of iron (0.27–0.61 Fe/f.u.) [53,54]. To model this mineral, a $1 \times 1 \times 3$ supercell (63 atoms) of NaMg$_2$(Al$_5$Si)O$_{12}$ is adopted. Various atomic configurations have been tested [55], and the most energetically favorable structure is shown in Fig. 1. This structure, consistent with previous calculations [52], has a helical screw axis with 3$_2$ symmetry along the [001] direction; the number of inequivalent atoms in the supercell is thus 21, not 63. The five inequivalent Al sites are labeled as Al1, Al4, Al7, Al10, and Al13 [Fig. 1(a)], where Al4, Al7, and Al10 are equivalent to Al5, Al9, and Al11 [Fig. 1(b)], respectively. The two inequivalent Mg sites are labeled as Mg1 and Mg4 [Fig. 1(a)], where Mg1 is equivalent to Mg2 and Mg3, and Mg4 is equivalent to Mg5 and Mg6 [Fig. 1(b)]. Each CO_6 double chain consists of one Si-free and one Si-containing column, shown as the Al1-Al5-Al9 and Al13-Al11-Si columns [Fig. 1(b)], respectively.

Inferred from Mössbauer spectra, three types of iron coexist in the NAL phase: Fe^{3+} occupying the C site, and Fe^{2+} and Fe^{3+} occupying the B site [36], referred to as C–Fe^{3+}, B–Fe^{2+}, and B–Fe^{3+}, respectively. To examine their SCO individually, three types of iron substitutions in a 63-atom
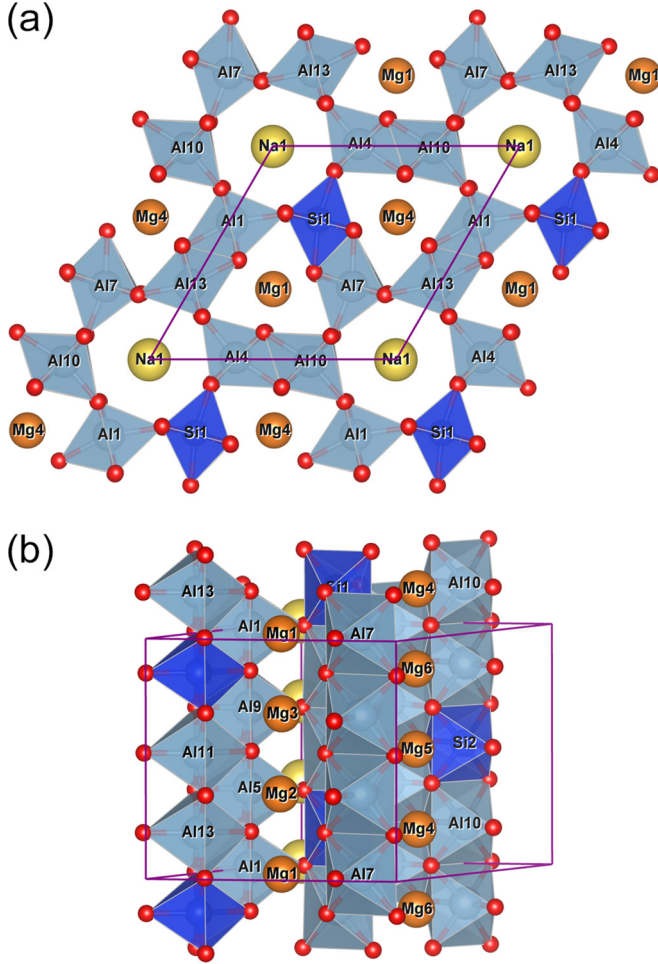
*hanhsu@ncu.edu.tw

FIG. 1. Atomic structure of the Fe-free NAL phase $NaMg_2(Al_5Si)O_{12}$. The atomic species and site numbers are labeled. (a) Top view; (b) side view.

TABLE I. The self-consistent Hubbard U (U_{sc}) of iron (in eV). U_{sc} depends on the oxidation state, spin state, and site occupancy [55].

	LS	IS	HS
B–Fe^{2+}	4.8	4.4	3.1
B–Fe^{3+}	5.3	4.4	3.7
C–Fe^{3+}	5.0	4.3	3.5

for Fe^{3+}). The U_{sc} of these states, listed in Table I, shows the same trend as in other minerals: U_{sc} decreases with S for a given valence/site, and B–Fe^{3+} has larger U_{sc} than B–Fe^{2+} [18,23,24,35,60,61]. For each type of iron substitution, the relative enthalpies of all inequivalent site occupancies and spin states are plotted in Fig. 2, with the ambient-pressure ground state as the reference. The results obtained with $U = 4$ eV [Figs. 2(a)–2(c)] and $U = U_{sc}$ [Figs. 2(d)–2(f)] are presented. Regardless of the choice of Hubbard U, both B–Fe^{2+} [Figs. 2(b) and 2(e)] and B–Fe^{3+} [Figs. 2(c) and 2(f)] remain in the HS state throughout the pressure range 0–80 GPa; only C–Fe^{3+} undergoes a HS-LS crossover while the IS state has a very high enthalpy [Figs. 2(a) and 2(d)]. The main difference between these two approaches is the predicted HS-LS transition pressure (P_T). With $U = 4$ eV, $P_T \approx 7$ GPa; with $U = U_{sc}$, $P_T \approx 47$ GPa. The latter is much closer to the room-temperature ($T = 300$ K) measurements: An anomalous volume reduction occurs in the pressure range 31–49 GPa [36]. All discussions hereafter will be based on the LDA+U_{sc} results.

Among the five inequivalent Al sites, HS C–Fe^{3+} prefers substituting Al1, Al5, and Al9 in the Si-free CO_6 column to Al11 and Al13, as indicated in Fig. 2(d). This tendency arises from the larger ionic radius of HS Fe^{3+} compared with Al^{3+} and Si^{4+}: The resultant larger FeO_6 octahedra disfavor sharing an edge with smaller SiO_6 octahedra. In contrast, LS Fe^{3+} has an ionic radius similar to Al^{3+}, so the five LS C–Fe^{3+} substitutions have nearly the same enthalpy [Fig. 2(d)]. Site occupancy can affect P_T as well. When Fe^{3+} substitutes Al1, Al5, and Al9 (Si-free CO_6 column), $P_T \approx 47$ GPa; when substituting Al11 or Al13, $P_T \approx 42$ GPa. The iron nuclear quadrupole splittings (QSs) ΔE_Q of the most favorable C–Fe^{3+}, B–Fe^{2+}, and B–Fe^{2+} substitutions are computed [55]. Throughout 0–80 GPa, HS C–Fe^{3+} has $\Delta E_Q = 0.52$–0.89, LS C–Fe^{3+} has $\Delta E_Q = 1.76$–1.80, HS B–Fe^{2+} has $\Delta E_Q = 3.56$–3.86, and HS B–Fe^{3+} has $\Delta E_Q = 1.15$–1.49 mm/s. These computed QSs, along with the enthalpy shown in Fig. 2, fully explain the observations in Mössbauer spectra [36]: An abrupt change in a QS from $\sim$0.6 to $\sim$1.8 mm/s in 30–40 GPa is a consequence of the HS-LS crossover of C–Fe^{3+}, while the other two QSs remaining at $\sim$3.6 and $\sim$1.9 mm/s throughout 0–80 GPa correspond to HS B–Fe^{2+} and HS B–Fe^{3+}, respectively.

In addition to $Fe^{3+}+Al^{3+} \Leftrightarrow Mg^{2+}+Si^{4+}$, the formation of B–Fe^{3+} can be also achieved via the coupled substitution $2Fe^{3+} \Leftrightarrow Mg^{2+}+Si^{4+}$, which yields $Na(Mg_{1.67}Fe_{0.33})(Al_5Si_{0.67}Fe_{0.33})O_{12}$. To investigate potential iron-iron interactions, three distinct configurations are considered: (1) Nearest-neighbored (NN) configuration with Fe^{3+} substituting Mg4 and Si1 (or equivalently, Mg5 and Si2), (2)

$NaMg_2(Al_5Si)O_{12}$ supercell are considered: (1) $Fe^{3+} \Leftrightarrow Al^{3+}$, yielding $NaMg_2(Al_{4.67}SiFe_{0.33})O_{12}$ with C–Fe^{3+}, (2) $Fe^{2+} \Leftrightarrow Mg^{2+}$, yielding $Na(Mg_{1.67}Fe_{0.33})(Al_5Si)O_{12}$ with B–Fe^{2+}, and (3) $Fe^{3+}+Al^{3+} \Leftrightarrow Mg^{2+}+Si^{4+}$, yielding $Na(Mg_{1.67}Fe_{0.33})(Al_{5.33}Si_{0.67})O_{12}$ with B–Fe^{3+}. While the formation of C–Fe^{3+} and B–Fe^{2+} only require simple substitution, the formation of B–Fe^{3+} requires coupled substitution (or reduced Si^{4+} concentration). With five and two inequivalent Al and Mg sites, respectively (Fig. 1), five and two inequivalent $Fe^{3+} \Leftrightarrow Al^{3+}$ and $Fe^{2+} \Leftrightarrow Mg^{2+}$ substitutions are considered. As to the $Fe^{3+}+Al^{3+} \Leftrightarrow Mg^{2+}+Si^{4+}$ coupled substitution, the (Fe^{3+}, Al^{3+}) pair is placed at the nearest-neighbored (Mg4,Si1) sites. To properly treat the on-site Coulomb interaction of the Fe-3d electrons, the local density approximation + self-consistent Hubbard U (LDA+U_{sc}) method is adopted, with the Hubbard U parameters computed from the first principles self-consistently [24,55–59]. Using this approach, SCO (or the lack thereof) in ferropericlase, bridgmanite, $MgSiO_3$ post-perovskite, and ferromagnesite have been successfully elucidated [18,23,24,35,60,61]. Within the LDA+U_{sc}, all types of iron in the NAL phase can be stabilized to high-spin (HS), intermediate-spin (IS), or low-spin (LS) states ($S = 2$, 1, and 0, respectively, for Fe^{2+}; $S = 5/2$, 3/2, and 1/2, respectively,
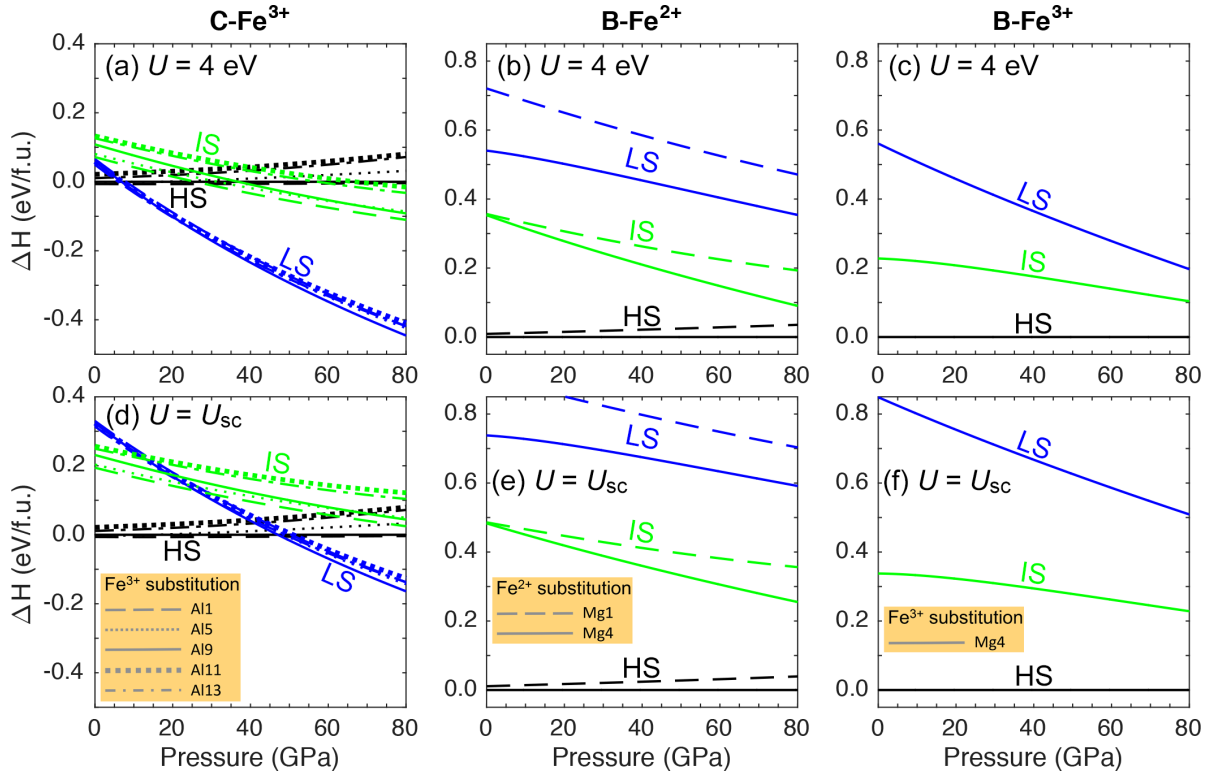
FIG. 2. Relative enthalpies of iron in various spin states residing in various inequivalent sites determined with (a)–(c) $U = 4$ eV and (d)–(f) $U = U_{sc}$. (a),(d) $NaMg_2(Al_{4.67}SiFe_{0.33})O_{12}$ (C–Fe^{3+}); (b),(e) $Na(Mg_{1.67}Fe_{0.33})(Al_5Si)O_{12}$ (B–Fe^{2+}); (c),(f) $Na(Mg_{1.67}Fe_{0.33})(Al_{5.33}Si_{0.67})O_{12}$ (B–Fe^{3+}). The numerical values of U_{sc} are listed in Table I.

far-apart configuration with Fe^{3+} substituting Mg3 and Si1 (or equivalently, Mg1 and Si2), and (3) far-apart configuration with Fe^{3+} substituting Mg4 and Al9, and Si1 replaced by Al^{3+}. In the NN configuration, the spin moments of the two Fe^{3+} can be parallel or antiparallel. Also, given that B–Fe^{3+} remains in the HS state, the spin states of these three configurations can be characterized solely by C–Fe^{3+} (HS or LS). As indicated by the relative enthalpies shown in Fig. 3,
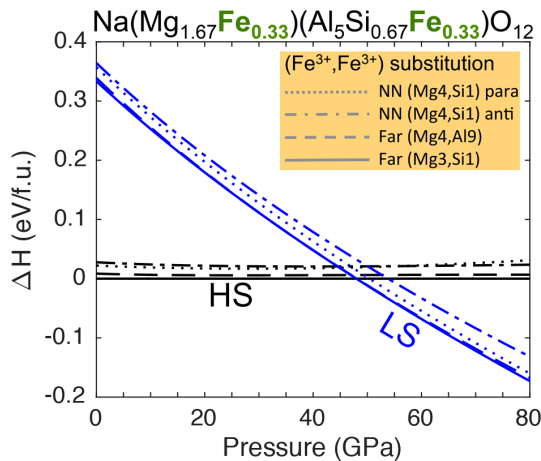

FIG. 3. Relative enthalpies of $Na(Mg_{1.67}Fe_{0.33})(Al_5Si_{0.67}Fe_{0.33})O_{12}$ with various (Fe^{3+},Fe^{3+}) substitutions and spin states. This result suggests that iron in the NAL phase tends to avoid neighboring with each other.

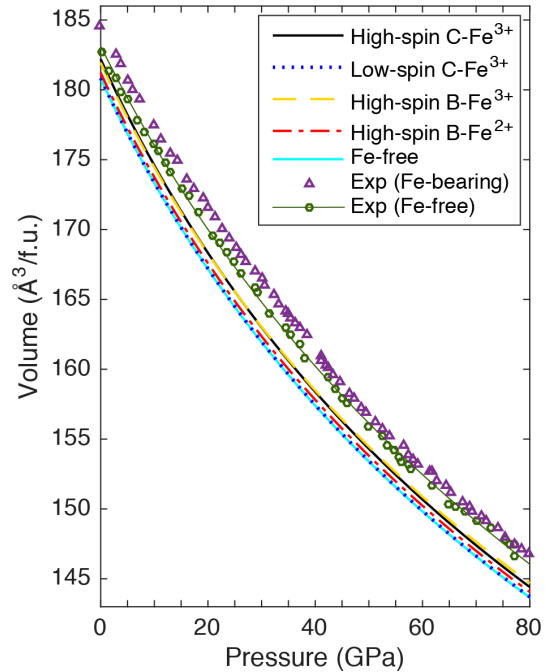FIG. 4. The LDA+U_{sc} compression curves of $NaMg_2(Al_5Si)O_{12}$ (Fe-free), $NaMg_2(Al_{4.67}SiFe_{0.33})O_{12}$ (C–Fe^{3+}), $Na(Mg_{1.67}Fe_{0.33})(Al_5Si)O_{12}$ (B–Fe^{2+}), and $Na(Mg_{1.67}Fe_{0.33})(Al_{5.33}Si_{0.67})O_{12}$ (B–Fe^{3+}) in the relevant spin states. Symbols are room-temperature measurements [36]. The raw data of the Fe-free sample (green circles) is fitted to the third-order Birch-Murnaghan equation of state (green solid thin line).

the two far-apart configurations, with nearly the same enthalpy, are more favorable than the NN configuration. In other words, iron atoms in the NAL phase tend to avoid neighboring with each other. Such a tendency could arise from the iron-iron interaction or from the unfavorable lattice distortion caused by nearest-neighboring iron.

Before further discussing SCO and the accompanying volume/elastic anomalies, the effects of iron substitution on the equation of state should be examined. In Fig. 4, the computed compression curves of the Fe-free and relevant Fe-bearing NAL phases (HS/LS C–Fe^{3+} and HS B–Fe^{2+}/Fe^{3+} in Fig. 2) are plotted, along with the room-temperature measurements [36]. All the computed curves are lower than the measured ones, as the LDA functional underestimates pressure. The computed equilibrium volume of the Fe-free NAL phase is 180.81 Å^3/f.u., smaller than the measured volume 183.10 Å^3/f.u. by $\sim$1.3%. This underestimate can be reduced by the inclusion of vibrational free energy. In

comparing the computed Fe-bearing and Fe-free curves, one single HS C–Fe^{3+} in a 63-atom supercell (equivalent to an increment of 0.33 HS C–Fe^{3+} per f.u.) increases the cell volume by 0.5%–0.8%. In contrast, LS C–Fe^{3+} causes nearly zero volume increase, as LS Fe^{3+} has about the same size as Al^{3+}. While the ionic radius of HS Fe^{2+} is larger than HS Fe^{3+}, the compression curve of HS B–Fe^{2+} is below HS C–Fe^{3+}. This is because the B site is located in the triangular-shaped tunnel, which is large enough to accommodate Fe^{2+} without significant lattice expansion. The compression curve of HS B–Fe^{3+} is slightly above that of HS B–Fe^{2+}. This larger volume, however, is not caused by B–Fe^{3+} itself, but by the higher Al^{3+} (lower Si^{4+}) concentration due to the coupled substitution $Fe^{3+}+Al^{3+} \Leftrightarrow Mg^{2+}+Si^{4+}$.

Given the low iron concentration in natural and synthesized samples (0.26–0.61 Fe/f.u., equivalent to 0.8–1.8 Fe/supercell) and the tendency that iron atoms avoid neighboring with each other, the Fe-bearing NAL phase
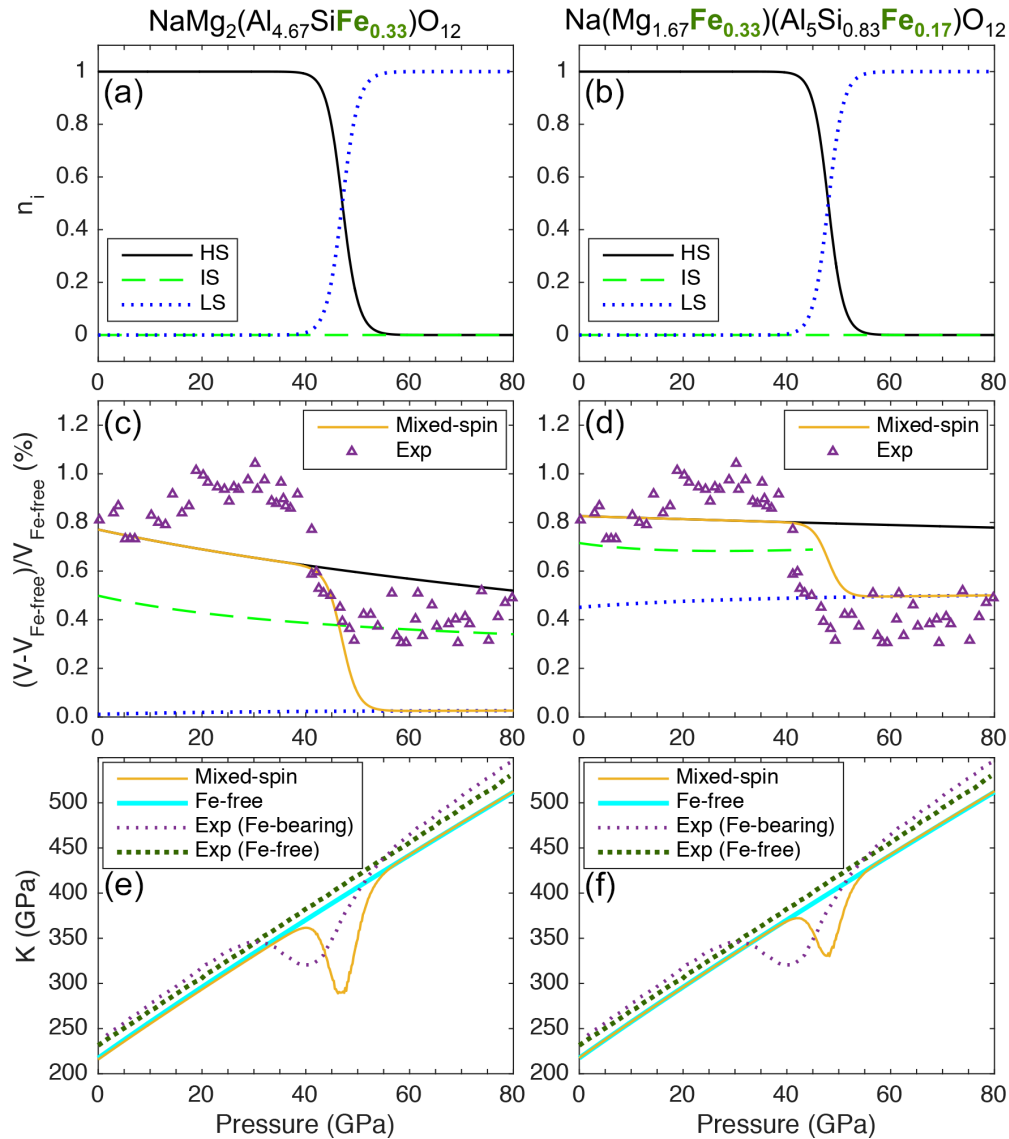

FIG. 5. Spin crossover and accompanying volume/elastic anomalies of $NaMg_2(Al_{4.67}SiFe_{0.33})O_{12}$ and $Na(Mg_{1.67}Fe_{0.33})(Al_5Si_{0.83}Fe_{0.17})O_{12}$ at room temperature. (a),(b) Fraction of HS, IS, and LS C-site Fe^{3+}; (c),(d) relative volume difference with respect to the Fe-free NAL phase; (e),(f) bulk modulus of the Fe-bearing and Fe-free NAL phase. Experiment results are adopted from Ref. [36].

can be modeled by a solid solution composed of the configurations discussed in Figs. 2 and 3. Using the most favorable configurations in these graphs, two distinct compositions are analyzed: $NaMg_2(Al_{4.67}SiFe_{0.33})O_{12}$ and $Na(Mg_{1.67}Fe_{0.33})(Al_5Si_{0.83}Fe_{0.17})O_{12}$. The former, shown in Fig. 2(d), contains only C–Fe^{3+}; the latter, a 1:1 mixture of $Na(Mg_{1.67}Fe_{0.33})(Al_5Si)O_{12}$ [Fig. 2(e)] and $Na(Mg_{1.67}Fe_{0.33})(Al_5Si_{0.67}Fe_{0.33})O_{12}$ (Fig. 3), contains B–Fe^{2+}, B–Fe^{3+}, and C–Fe^{3+}. When the temperature $T \neq 0$, spin crossover of the C-site Fe^{3+} goes through a mixed-spin phase within a finite pressure range. Without including the vibrational free energy, the fraction n_i of C–Fe^{3+} in spin state i ($i =$ LS, IS, or HS) in the mixed-spin phase can be estimated using Eq. (1) with the constraint $\sum_i n_i = 1$ [14,62]:

$$\frac{n_i}{n_{HS}} = \frac{m_i(2S_i+1)}{m_{HS}(2S_{HS}+1)} \exp\left(-\frac{\Delta H_i}{k_B T x}\right), \quad (1)$$

where m_i and S_i are the orbital degeneracy and total electron spin of spin state i, respectively, and x is the concentration of the C–Fe^{3+}. For C–Fe^{3+}, the HS state ($t_{2g}^3 e_g^2$) has only one orbital configuration, therefore, $m_{HS} = 1$. The LS state ($t_{2g}^5 e_g^0$), in contrast, has three possible orbital configurations: a t_{2g} hole in the d_{xy}, d_{yz}, or d_{xz} orbital. Since FeO_6 octahedra are distorted, these three LS configurations are nondegenerate. While the LDA+U_{sc} wave function tends to converge to the most favorable LS configuration, the lower and upper limits of LS fraction n_{LS} can be determined using $m_{LS} = 1$ and 3, respectively. Nevertheless, the energy splittings between the three LS states are small, so $m_{LS} = 3$ would be more accurate. To compare with room-temperature experiments [36], the computed fraction n_i (with $T = 300$ K and $m_{LS} = 3$), relative volume difference with respect to the Fe-free NAL phase, and bulk modulus K, are plotted in Fig. 5. Both compositions go through a HS-LS crossover in the pressure range 40–54 GPa, with the transition pressure $P_T \approx 47$ GPa [Figs. 5(a) and 5(b)], where P_T is defined by $n_{LS}(P_T) = n_{HS}(P_T) = 0.5$ when $T \neq 0$. The computed SCO has nearly the same width as the measured SCO (31–49 GPa), but P_T is ~7 GPa higher, as can be seen in the anomalous volume reduction [Figs. 5(c) and 5(d)] and bulk modulus softening [Figs. 5(e) and 5(f)]. For $NaMg_2(Al_{4.67}SiFe_{0.33})O_{12}$, the relative volume difference changes from 0.62% to 0.03% [Fig. 5(c)], indicating an anomalous volume reduction of ~0.6% accompanying the SCO. In experiments, the Fe-bearing sample has a volume reduction of ~0.45% (from 0.85% to 0.4%). Based on the discussion for Fig. 4, $NaMg_2(Al_{4.67}SiFe_{0.33})O_{12}$ contains more C–Fe^{3+} and less B–Fe^{2+}/Fe^{3+} than the sample. In contrast, $Na(Mg_{1.67}Fe_{0.33})(Al_5Si_{0.83}Fe_{0.17})O_{12}$ undergoes a volume change from 0.80% to 0.50% [Fig. 5(d)], in great agreement with experiments. Likewise, the anomalous bulk modulus softening observed in $NaMg_2(Al_{4.67}SiFe_{0.33})O_{12}$ [Fig. 5(e)] is twice larger than in $Na(Mg_{1.67}Fe_{0.33})(Al_5Si_{0.83}Fe_{0.17})O_{12}$ [Fig. 5(f)], while the latter is also in great agreement with experiment. Indeed, the nominal iron concentration of the sample is 0.26 Fe/f.u. [36], lower than in $Na(Mg_{1.67}Fe_{0.33})(Al_5Si_{0.83}Fe_{0.17})O_{12}$ (0.5 Fe/f.u.). However, our previous LDA+U_{sc} calculation of $(Mg_{1-x}Fe_x)CO_3$ has shown that theory can accurately determine the volume/elastic anomalies throughout $0.125 \leqslant x \leqslant 1$ [35]. The
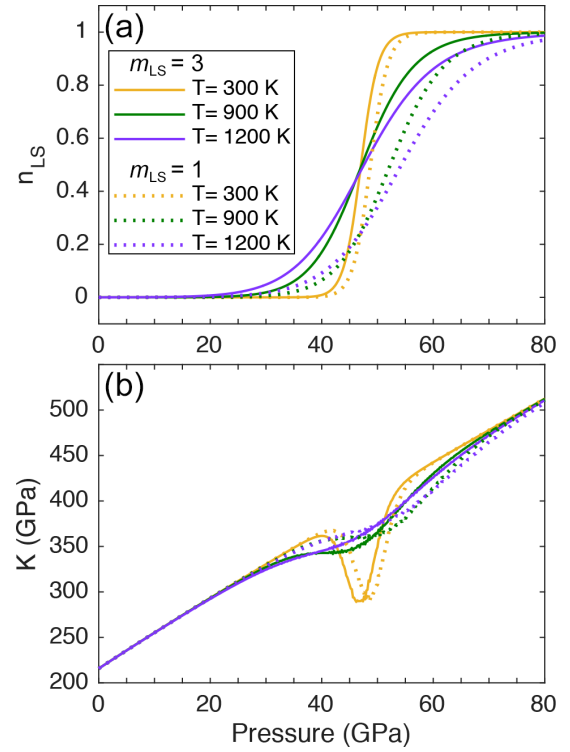

FIG. 6. Elastic anomalies of the NAL phase in natural MORB at high temperatures. (a) Fraction of LS C–Fe^{3+}; (b) bulk modulus. The NAL phase can be more accurately described by $m_{LS} = 3$.

above-mentioned discrepancy is thus more likely to result from the uncertainty in sample characterization.

Based on Refs. [53,54], the NAL phase in natural MORB contains 0.27–0.61 Fe/f.u. and 1.85–2.13 Mg/f.u., suggesting a significant portion of iron occupying the C site, approximately 0.2–0.4 C–Fe^{3+}/f.u. A similar analysis for another natural sample with ~1 Fe/f.u. suggests the same [63]. Given that the elastic anomalies accompanying SCO are mainly determined by C–Fe^{3+}, $NaMg_2(Al_{4.67}SiFe_{0.33})O_{12}$ with 0.33 C–Fe^{3+}/f.u. [Fig. 5(e)] can be used to estimate the NAL phase's elastic anomalies in the lower mantle. Using Eq. (1), the fraction of LS C–Fe^{3+} (n_{LS}) and bulk modulus (K) at various temperatures are plotted in Fig. 6, where 900 and 1200 K are the estimated temperatures of the subducted slab at the top of the lower mantle based on different geophysical models [39,54]. The effects of orbital degeneracy m_{LS} are also examined. At $T = 300$ K, m_{LS} barely affects n_{LS} and K; at higher temperatures, the effects of m_{LS} become more significant, as m_{LS} is associated with the magnetic entropy, contributing to the Gibbs free energy in the form of $-k_BT \log m_{LS}$ [14,62]. With $m_{LS} = 1$, both P_T and the width of SCO drastically increase with T; with $m_{LS} = 3$, P_T almost remains constant, and the width of SCO moderately increases with T. Furthermore, the elastic anomalies are still very prominent at $T = 900$ and 1200 K with $m_{LS} = 3$, starting at as low as ~35 GPa [Fig. 6(b)]. Since the NAL phase is more accurately described by $m_{LS} = 3$ and the LDA+U_{sc} method overestimates P_T by 5–10 GPa (see Fig. 5 and Ref. [35]), the *actual* elastic anomalies of the NAL phase under high temperature can be expected to start at $P \lesssim 30$ GPa, namely, the top lower mantle. In contrast, ferroper-

iclase and ferromagnesite have LS Fe^{2+} with $m_{LS} = 1$; their elastic anomalies occur in the mid-lower mantle [8,11,35].

In summary, iron spin crossover in the NAL phase is revealed by a series of LDA+U_{sc} calculations. Only the Fe^{3+} substituting Al/Si in the octahedral (C) site undergoes a crossover from the high-spin to the low-spin state at ~40 GPa at room temperature; iron substituting Mg in the trigonal-prismatic (B) site remains in the high-spin state, regardless of its oxidation state. All the major calculation results, including the transition pressure, abrupt increase in iron nuclear quadrupole splitting (from 0.6 to 1.8 mm/s), and volume/elastic anomalies, are in great agreement with room-temperature experiments. The calculations further predict that the transition pressure of the NAL phase barely increases with temperature due to the three nearly degenerate LS states of the C-site Fe^{3+}, suggesting that the elastic anomalies accompanying iron spin crossover can occur at the top lower mantle, in contrast to ferropericlase and ferromagnesite.

[1] J. Badro, G. Fiquet, F. Guyot, J. Rueff, V. Struzhkin, G. Vanko, and G. Monaco, Science **300**, 789 (2003).

[2] J.-F. Lin, V. V. Struzhkin, S. D. Jacobsen, M. Y. Hu, P. Chow, J. Kung, H. Liu, H.-k. Mao, and R. J. Hemley, Nature (London) **436**, 377 (2005).

[3] S. Speziale, A. Milber, V. E. Lee, S. M. Clark, M. P. Pasternak, and R. Jeanloz, Proc. Natl. Acad. Sci. USA **102**, 17918 (2005).

[4] T. Tsuchiya, R. M. Wentzcovitch, C. R. S. da Silva, and S. de Gironcoli, Phys. Rev. Lett. **96**, 198501 (2006).

[5] A. F. Goncharov, V. V. Struzhkin, and S. D. Jacobsen, Science **312**, 1205 (2006).

[6] J.-F. Lin, G. Vanko, S. D. Jacobsen, V. Iota, V. V. Struzhkin, V. B. Prakapenka, A. Kuznetsov, and C.-S. Yoo, Science **317**, 1740 (2007).

[7] J. Crowhurst, J. M. Brown, A. F. Goncharov, and S. D. Jacobsen, Science **319**, 451 (2008).

[8] R. M. Wentzcovitch, J. F. Justo, Z. Wu, C. R. S. da Silva, D. A. Yuen, and D. Kohlstedtd, Proc. Natl. Acad. Sci. USA **106**, 8447 (2009).

[9] H. Marquardt, S. Speziale, H. J. Reichmann, D. J. Frost, F. R. Schilling, and E. J. Garnero, Science **324**, 224 (2009).

[10] D. Antonangeli, J. Siebert, C. M. Aracne, D. L. Farber, A. Bosak, M. Hoesch, M. Krisch, F. J. Ryerson, G. Fiquet, and J. Badro, Science **331**, 64 (2011).

[11] Z. Wu, J. F. Justo, and R. M. Wentzcovitch, Phys. Rev. Lett. **110**, 228501 (2013).

[12] E. Holmstrom and L. Stixrude, Phys. Rev. Lett. **114**, 117202 (2015).

[13] Z. Wu and R. M. Wentzcovitch, Proc. Natl. Acad. Sci. USA **111**, 10468 (2014).

[14] H. Hsu, K. Umemoto, Z. Wu, and R. M. Wentzcovitch, Rev. Mineral. Geochem. **71**, 169 (2010).

[15] R. M. Wentzcovitch, H. Hsu, and K. Umemoto, Eur. J. Mineral. **24**, 851 (2012).

[16] J.-F. Lin, S. Speziale, Z. Mao, and H. Marquardt, Rev. Geophys. **51**, 244 (2013).

[17] J. Badro, Annu. Rev. Earth Planet. Sci. **42**, 231 (2014).

[18] H. Hsu and R. M. Wentzcovitch, Phys. Rev. B **90**, 195205 (2014).

[19] J. Badro, J. Rueff, G. Vanko, G. Monaco, G. Fiquet, and F. Guyot, Science **305**, 383 (2004).

[20] J. Li, V. V. Struzhkin, H.-k. Mao, J. Shu, R. J. Hemley, Y. Fei, B. Mysen, P. Dera, V. Prakapenka, and G. Shen, Proc. Natl. Acad. Sci. USA **101**, 14027 (2004).

[21] C. McCammon, I. Kantor, O. Narygina, J. Rouquette, U. Ponkratz, I. Sergueev, M. Mezouar, V. Prakapenka, and L. Dubrovinsky, Nat. Geosci. **1**, 684 (2008).

[22] J.- F Lin, H. Watson, G. Vanko, E. E. Alp, V. B. Prakapenka, P. Dera, V. Struzhkin, A. Kubo, J. Zhao, C. McCammon, and W. J. Evans, Nat. Geosci. **1**, 688 (2008).

[23] H. Hsu, K. Umemoto, P. Blaha, and R. M. Wentzcovitch, Earth Planet. Sci. Lett. **294**, 19 (2010).

[24] H. Hsu, P. Blaha, M. Cococcioni, and R. M. Wentzcovitch, Phys. Rev. Lett. **106**, 118501 (2011).

[25] V. Potapkin, C. McCammon, K. Glazyrin, A. Kantor, I. Kupenko, C. Prescher, R. Sinmyo, G. V. Smirnov, A. I. Chumakov, R. Rüffer, and L. Dubrovinsky, Nat. Commun. **4**, 1427 (2013).

[26] A. Mattila, T. Pylkkanen, J-P. Rueff, S. Huotari, G. Vanko, M. Hanfland, M. Lehtinen, and K. Hamalainen, J. Phys.: Condens. Matter **19**, 386206 (2007).

[27] B. Lavina, P. Dera, R. T. Downs, V. Prakapenka, M. Rivers, S. Sutton, and M. Nicol, Geophys. Res. Lett. **36**, L23306 (2009).

[28] T. Nagai, T. Ishido, Y. Seto, D. Nishio-Hamane, N. Sata, and K. Fujino, J. Phys.: Conf. Ser. **215**, 012002 (2010).

[29] B. Lavina, P. Dera, R. T. Downs, O. Tschauner, W. Yang, O. Shebanova, and G. Shen, High Press. Res. **30**, 224 (2010).

[30] B. Lavina, P. Dera, R. T. Downs, W. Yang, S. Sinogeikin, Y. Meng, G. Shen, and D. Schiferl, Phys. Rev. B **82**, 064110 (2010).

[31] J.-F. Lin, J. Liu, C. Jacobs, and V. Prakapenka, Am. Mineral. **97**, 583 (2012).

[32] G. Farfan, S. Wang, H. Ma, R. Caracas, and W. L. Mao, Am. Mineral. **97**, 1421 (2012).

[33] J. Liu, J.-F. Lin, Z. Mao, and V. Prakapenka, Am. Mineral. **99**, 84 (2014).

[34] S. S. Lobanov, A. F. Goncharov, and K. D. Litasov, Am. Mineral. **100**, 1059 (2015).

[35] H. Hsu and S. C. Huang, Phys. Rev. B **94**, 060404(R) (2016).

[36] Y. Wu, X. Wu, J.-F. Lin, C. A. McCammond, Y. Xiao, P. Chow, V. B. Prakapenka, T. Yoshino, S. Zhai, and S. Qin, Earth Planet. Sci. Lett. **434**, 91 (2016).

[37] K. Hirose, Y. Fei, Y. Ma, and H.-K. Mao, Nature (London) **397**, 53 (1999).

[38] G. R. Helffrich and B. J. Wood, Nature (London) **412**, 501 (2001).

[39] Y. Ricard, E. Mattern, and J. Matas, *Earth's Deep Mantle: Structure, Composition, and Evolution*, edited by R. D. Van Der Hilst, J. D. Bass, J. Matas, and J. Trampert, Geophysical Monograph Series Vol. 160 (American Geophysical Union, 2005), p. 285.

[40] K. Ohta, K. Hirose, T. Lay, N. Sata, and Y. Ohishi, Earth Planet. Sci. Lett. **267**, 107 (2008).

[41] L. Stixrude and C. Lithgow-Bertelloni, Annu. Rev. Earth Planet. Sci. **40**, 569 (2012).

[42] T. Irifube and A. E. Ringwood, Earth Planet. Sci. Lett. **117**, 101 (1993).

[43] M. Akaogi, Y. Hamada, T. Suzuki, M. Kobayashi, and M. Okada, Phys. Earth Planet. Inter. **115**, 67 (1999).

[44] N. Miyajima, K. Fujino, N. Funamori, T. Kondo, and T. Yagi, Phys. Earth Planet. Inter. **116**, 117 (1999).

[45] H. Miura, Y. Hamada, T. Suzuki, M. Akaogi, N. Miyajima, and K. Fujino, Am. Mineral. **85**, 1799 (2000).

[46] N. Guignot and D. Andrault, Phys. Earth Planet. Inter. **143-144**, 107 (2004).

[47] K. Hirose, N. Takafuji, N. Sata, and Y. Ohishi, Earth Planet. Sci. Lett. **237**, 239 (2005).

[48] A. Ono, M. Akaogi, H. Kojitani, K. Yamashita, and M. Kobayashi, Phys. Earth Planet. Inter. **174**, 39 (2009).

[49] L. Dai, Y. Kudo, K. Hirose, M. Murakami, Y. Asahara, H. Ozawa, Y. Ohishi, and N. Hirao, Phys. Chem. Miner. **40**, 195 (2013).

[50] M. G. Pamato, A. Kurnosov, T. B. Ballaran, D. M. Trots, R. Caracas, and D. J. Frost, Am. Mineral. **99**, 1562 (2014).

[51] S. Imada, K. Hirose, and Y. Ohishi, Phys. Chem. Minerals **38**, 557 (2011).

[52] K. Kawai and T. Tsuchiya, Am. Mineral. **97**, 305 (2012).

[53] A. Ricolleau, G. Fiquet, A. Addad, N. Menguy, C. Vanni, J.-P. Perrillat, I. Daniel, H. Cardon, and N. Guignot, Am. Mineral. **93**, 144 (2008).

[54] A. Ricolleau, J.-P. Perrillat, G. Fiquet, I. Daniel, J. Matas, A. Addad, N. Menguy, H. Cardon, M. Mezouar, and N. Guignot, J. Geophys. Res. **115**, B08202 (2010).

[55] See Supplemental Material at http://link.aps.org/supplemental/10.1103/PhysRevB.95.020406 for the atomic structure of the $AB_2C_6O_{12}$ NAL phase, the computation method, and the hyperfine parameters of iron.

[56] M. Cococcioni and S. de Gironcoli, Phys. Rev. B **71**, 035105 (2005).

[57] H. J. Kulik, M. Cococcioni, D. A. Scherlis, and N. Marzari, Phys. Rev. Lett. **97**, 103001 (2006).

[58] B. Himmetoglu, R. M. Wentzcovitch, and M. Cococcioni, Phys. Rev. B **84**, 115108 (2011).

[59] B. Himmetoglu, A. Floris, S. Gironcoli, and M. Cococcioni, Int. J. Quantum Chem. **114**, 14 (2014).

[60] Y. G. Yu, H. Hsu, M. Cococcioni, and R. M. Wentzcovitch, Earth Planet. Sci. Lett. **331-332**, 1 (2012).

[61] H. Hsu, Y. G. Yu, and R. M. Wentzcovitch, Earth Planet. Sci. Lett. **359-360**, 34 (2012).

[62] K. Umemoto, H. Hsu, and R. M. Wentzcovitch, Phys. Earth Planet. Inter. **180**, 209 (2010).

[63] M. J. Walter, S. C. Kohn, D. Araujo, G. P. Bulanova, C. B. Smith, E. Gailou, J. Wang, A. Steele, and S. B. Shirey, Science **334**, 54 (2011).